

Dynamic Programing on a Tree for Ultrasound Elastography

Roozbeh Shams^a, Mathieu Boily^b, Paul A. Martineau^{b,c}, and Hassan Rivaz^{a,c}

^aDepartment of Electrical and Computer Engineering, Concordia University, Montreal, Canada

^bMcGill University Health Centre (MUHC), Montreal, Canada

^cPERFORM Centre, Concordia University, Montreal, Canada

ABSTRACT

Ultrasound Elastography is an emerging imaging technique that allows estimation of the mechanical characteristics of tissue. Two issues that need to be addressed before widespread use of elastography in clinical environments are real time constraints and deteriorating effects of signal decorrelation between pre- and post-compression images. Previous work has used Dynamic Programming (DP) to estimate tissue deformation. However, in case of large signal decorrelation, DP can fail. In this paper we, have proposed a novel solution to this problem by solving DP on a tree instead of a single Radio-Frequency line. Formulation of DP on a tree allows exploiting significantly more information, and as such, is more robust and accurate. Our results on phantom and *in-vivo* human data show that DP on tree significantly outperforms traditional DP in ultrasound elastography.

Keywords: Dynamic Programming, Ultrasound Imaging, Ultrasound Elastography

1. INTRODUCTION

Ultrasound elastography involves imaging mechanical properties of tissue by estimating tissue deformation due to external or internal sources of deformation.¹ Elastography has evolved into many different variations with promising results. The focus of this work is on palpation quasi-static elastography, where the probe is hand-held and tissue is compressed by manually pressing the ultrasound probe. Analyzing the pre- and post-compression ultrasound images yields a deformation map, which is then used to estimate strain images. Palpation elastography does not require any special equipment, and as such, it can be conveniently used in both diagnosis and surgical planning. However, there are challenges to overcome before it can be widely used for clinical purposes. Two major issues that need to be addressed are real time constraints and effects of signal decorrelation between pre-compression and post-compression images.

Accurate and robust estimation of the displacement field is an active field of research. A stochastic approach is taken in Ref. 2 where Kalman filtering based on bio-mechanical properties of the tissue is used to generate strain images. Rivaz et al. introduced a new method in Ref. 4 for generating strains using three (or multiple) frames. This was done by deriving constraints on variation of the displacement field and by solving a minimization problem constructed based on these constraints. Kuzmin et al. have proposed a method in Ref. 3 which uses three Radio-Frequency (RF) data frames acquired with a force-controlled ultrasound probe. The calculated displacement from the first two frames is used to improve the accuracy of the displacement calculation of the first and third frame. A different approach is taken in Ref. 5 in which a one-prediction-one-correction method is developed for dynamically choosing the pre- and post-compression images in real-time.

Jiang and Hall⁶ and Rivaz et al.⁷ proposed Dynamic Programming (DP) for real-time displacement estimation. In Ref. 8, Rivaz et al. proposed a method using DP and Analytic Minimization (AM) of a cost function to estimate the displacement field. An integer displacement (ID) field for a single RF-line is first calculated using DP, which is then refined using the AM step. An issue with this technique is that the DP solution can be incorrect if there is large decorrelation between pre- and post-compression images. Fleming et al.⁹ therefore proposed to improve this work by running DP multiple times and selecting the best outcome. While this work significantly improves the performance, it only uses single RF-lines for DP optimization, and does not *group* multiple RF-lines to utilize their information.

In this paper, we propose a technique where DP is estimated on a tree instead of a single RF-line. DP on a tree allows us to exploit data from multiple RF-lines to improve the reliability of ID field estimated from DP.

We call our method Elastography using Dynamic Programming On a Tree (EDPOT). This paper is summarized as follows. In the next section, we illustrate the technical details of our algorithm. We then show the results on phantom and *in-vivo* human data, and provide conclusions and avenues for future work.

2. METHODS

Let \mathbf{I}_1 and \mathbf{I}_2 to be pre- and post-compression ultrasound images with the size $m \times n$. The goal is to calculate the matrices \mathbf{A} and \mathbf{L} such that A_{ij} and L_{ij} are the axial and lateral displacements for pixel (i, j) of the ultrasound image. The method used to calculate \mathbf{A} and \mathbf{L} can be broken down to two main steps. First, for one RF-line (the seed-line), ID is calculated. In the AM step, sub-integer and accurate displacement is calculated based on the ID for the seed-line. The displacement of the seed-line is used as an initial estimate for neighboring lines and is refined using AM. This procedure is then propagated until the displacement of the entire image is estimated.

Erroneous DP results create distinct artifacts in the strain images as shown in Figure 1. Since the displacement is propagated from the seed-line, the accuracy of the displacement field calculated for that line is crucial. The outcome of DP for the seed-line itself very much depends on the RF-line chosen as the seed-line; for the seed-lines whose out-of-plane and lateral motion is large, DP will likely fail.

The focus of this work is on the first step so to improve the DP estimation of the initial ID. In this section we will describe the required steps for generating the strain image which can be summarized as following:

1. Calculating Integer Displacement
 - (a) Designing a tree to calculate the ID
 - (b) Constructing a recursive cost function for pixels on the said tree
 - (c) Using DP to find the optimum displacements
 - (d) Choosing a path on the tree with the most accurate displacement
2. Calculating Sub-sample displacement
 - (a) Deriving the sub sample displacement of the seed-line by means of AM
 - (b) Using the sub sample displacement of the seed-line as an estimate for calculating the displacement of the neighboring RF-lines and propagating the displacement
 - (c) Calculating the gradient of the displacement map to acquire the strain image

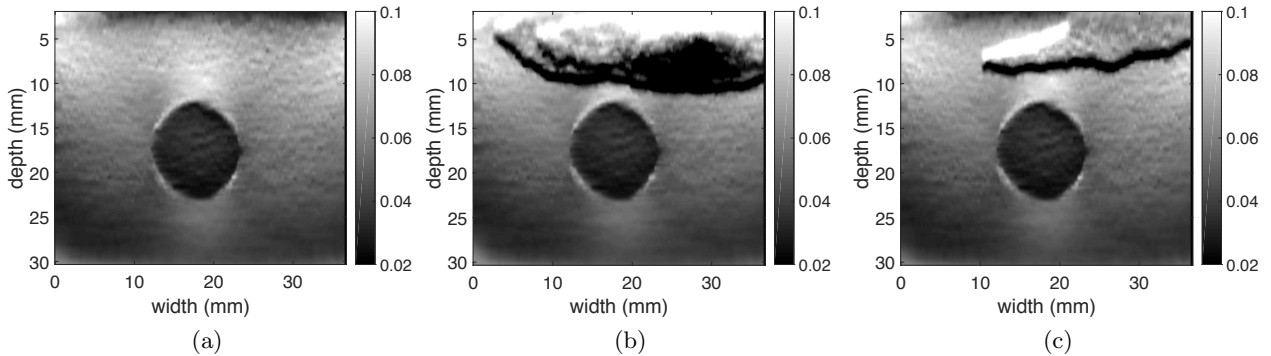


Figure 1: Strain images of a tissue mimicking phantom. A correct strain image is shown in (a), and two examples of incorrect strain images are shown in (b) and (c). The long dark band in the top part of (b) and (c) is artifact and is caused by failure in DP.

2.1 Integer Displacement Calculation

Our underlying goal is to exploit more information in the RF data. To achieve this goal, not only the information in the potential seed-line is used, but also the information in the neighboring lines is utilized. A general solution to discrete global optimization of a cost function that considers 4 neighbors of a pixel in the regularization term is NP-hard¹⁰ and therefore is computationally intractable.

To overcome this issue, it has been proposed to formulate DP on a tree to take advantage of more information.¹⁰ We adopt a similar approach and calculate DP on a tree instead of a single RF-line. Figure 2 shows DP on a single seed-line in left, and our proposed method that estimates DP on a tree in right. For this study we have chosen a relatively simple tree topology (Figure 2). It includes three edges E_1 , E_2 and E_3 : one stretching from the top of the image to a joint pixel (V_1), and two from the joint pixel to the bottom of the image on left and right (E_2 and E_3). The parameters involving this structure are the length of E_1 and the distance between E_2 and E_3 .

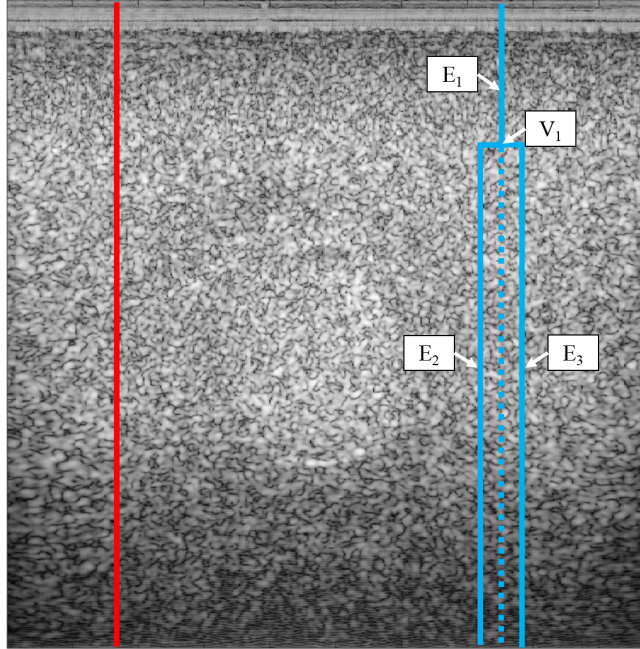


Figure 2: Calculating DP on a line versus on a tree.

We have empirically chosen l_{E_1} to be 150 pixels where a good balance is struck between overall improvement and computational complexity. In our tests, changing this parameter did not result in significant variation in the results; however optimizing l_{E_1} can be the subject of a future study. In an extreme case which E_1 starts from the top and finishes at the bottom, the tree will be reduced to one line and we will get the same result as Ref. 8. In another extreme case where l_{E_1} is 0, the tree structure will be two parallel lines. Choosing a more complex tree structure could lead to a more efficient way of utilizing available information. The next step after deciding on the tree structure is to calculate the ID on the tree. In this regard, we construct a cost function:

$$C(a_i, l_i, i, j) = \Delta(i, j, a_i, l_i) + \min_{\delta_a, \delta_l} \{C(\delta_a, \delta_l, i-1, j) + wS(a_i, l_i, a, l)\}, \quad (1)$$

where

$$\Delta(i, j, a_i, l_i) = |I_1(i, j) - I_2(i + a_i, j + l_i)|, \quad (2)$$

and

$$S(a_i, l_i, a_{(i-1)}, l_{(i-1)}) = |a_i - a_{(i-1)}| + |l_i - l_{i-1}|. \quad (3)$$

Δ is the data term and S is the regularization term of the cost function, C . i and j are integers from 1 to m and 1 to n respectively. a_i and l_i are the axial and lateral displacement at sample i of the seed-line. Also, w is the regularization weight which determines the smoothness of the calculated displacement function. We use DP to optimize this cost function on the tree structure and generate the ID estimates of the seed tree.

Assume P_1 and P_2 to be two paths on the tree: P_1 is the path including E_1 and E_2 and P_2 is the path including E_1 and E_3 . The next step involves choosing the path wherein a more accurate ID can be calculated. Veksler¹⁰ considers the cost value at V_1 for each path and chooses the path with smaller cost. However, our result showed that this approach does not necessarily select the best path in ultrasound images due to the following reason. The value of C heavily depends on US intensity values, which are highly dependent on tissue echogeneity. Therefore, we propose an novel approach as following. The optimum ID is first calculated for the pixels on E_2 and E_3 . Let (i_2, j_{max}) and (i_3, j_{max}) be the coordinates of the pixels on E_2 and E_3 which are on the same row and the calculated ID for them, differ the most:

$$j_{max} = \underset{j}{\operatorname{argmax}} |a_{E_2}(i_2, j) - a_{E_3}(i_3, j)| \quad (4)$$

where a_{E_2} and a_{E_3} are the calculated axial displacements on E_2 and E_3 and i_2 and i_3 are the column indexes for pixels on E_2 and E_3 . We then calculate NCC_2 and NCC_3 for the mentioned points on E_2 and E_3 respectively:

$$NCC_e = \sum_{x,y} \frac{(w_1(x,y) - \bar{w}_1)(w_2(x,y) - \bar{w}_2)}{\sigma_{w_1} \sigma_{w_2}} \quad (5)$$

where w_1 and w_2 are 9×5 windows, centered at (i_e, j_{max}) and $(i_e + a_{i_e, j_{max}}, j_{max} + l_{i_e, j_{max}})$ in I_1 and I_2 respectively. The path which contains the point with higher NCC, will be chosen and the ID of this path will be used for the next steps. An issue is that DP only provides ID, and as such, is not very accurate. RF data is the result of modulation of a high-frequency carrier signal with an input signal and therefore, NCC can change significantly even with a small shift of the window (Figure 3). Moreover, presence of small errors in ID is inevitable due to it being integer. Therefore the changes in NCC with small shifts renders NCC of RF data ineffective, and therefore, we use envelope data in Equation 5. In the final step, the ID on the core seed-line (dotted line in Figure 2) is estimated based on the displacement calculated on the chosen branch. This displacement is then used in the next step.

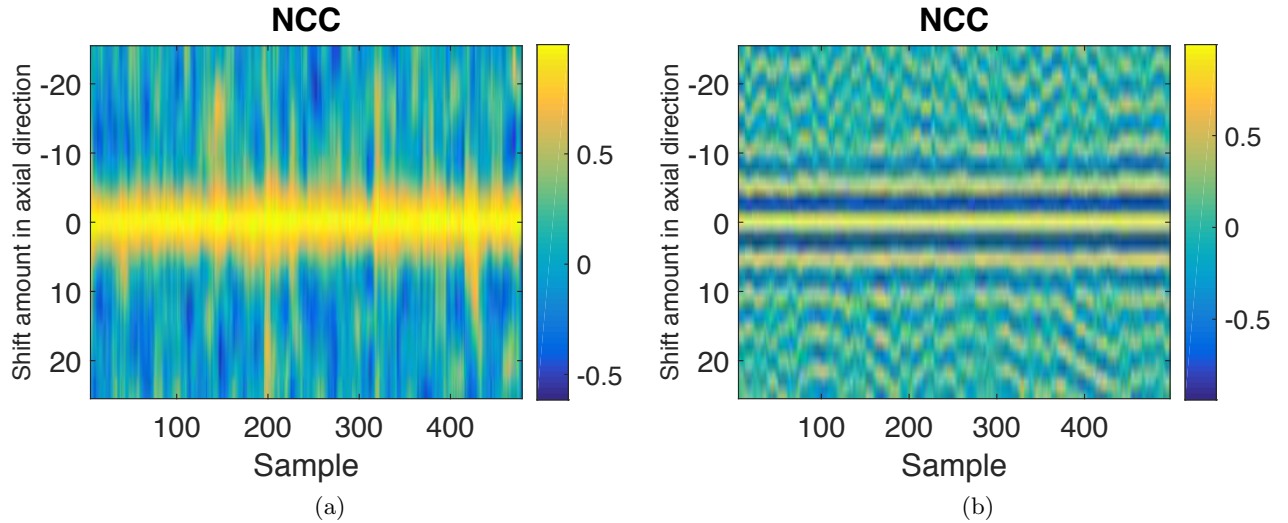


Figure 3: NCC values of experimental phantom data. (a) shows the NCC for a 9×5 window with vertical shifts for pixels of a single row of the envelope data, (b) shows the same for the raw Rf data. The effect of the carrier wave is clearly visible in (b).

2.2 Subsample Displacement Calculation

In this step, subsample displacement (SD) is first calculated for the core seed-line and propagated to the left and right using SD of the previous RF-line as the initial displacement. Therefore, for one line at a time, the goal is to find the optimum Δa_i and Δl_i which make the duple $(a_i + \Delta a_i, l_i + \Delta l_i)$ the optimum solution for the following function:

$$C(\Delta a_1, \dots, \Delta a_m, \Delta l_1, \dots, \Delta l_m) = \sum_{i=1}^m \{ [I_1(i, j) - I_2(i + a_i + \Delta a_i, j + a_j + \Delta l_j)]^2 + \alpha(a_i + \Delta a_i - a_{i-1} - \Delta a_{i-1})^2 + \beta_a(l_i + \Delta l_{i-1} - \Delta l_{i-1})^2 + \beta'_l(l_i + \Delta l_i - l_{i,j-1})^2 \}, \quad (6)$$

where $l_{i,j-1}$ is the lateral displacement of the previous line and α , β_a and β'_l are the regularization terms. Considering the cost is calculated for each RF-line separately, we have dropped the index j . Hence a_i , l_i , Δa_i and Δl_i are in fact $a_{i,j}$, $l_{i,j}$, $\Delta a_{i,j}$ and $\Delta l_{i,j}$.

Using this cost function, the SD is calculated first for the core seed-line by choosing the ID as the initial estimate. Next, the same procedure will be carried out for the line on the left and on the right of the core seed-line and like so for every other line; except the SD of the previous line is used as the initial estimate. In the end, the strain image can be calculated by taking the gradient of the displacement fields and applying appropriate filtering technique to increase the quality.

3. RESULTS

We tested ED POT on phantom and *in-vivo* human data. The human data is composed of RF data of the liver from patients with liver cancer, as well as B-mode images of patellar tendon. These datasets are further described in corresponding sections below.

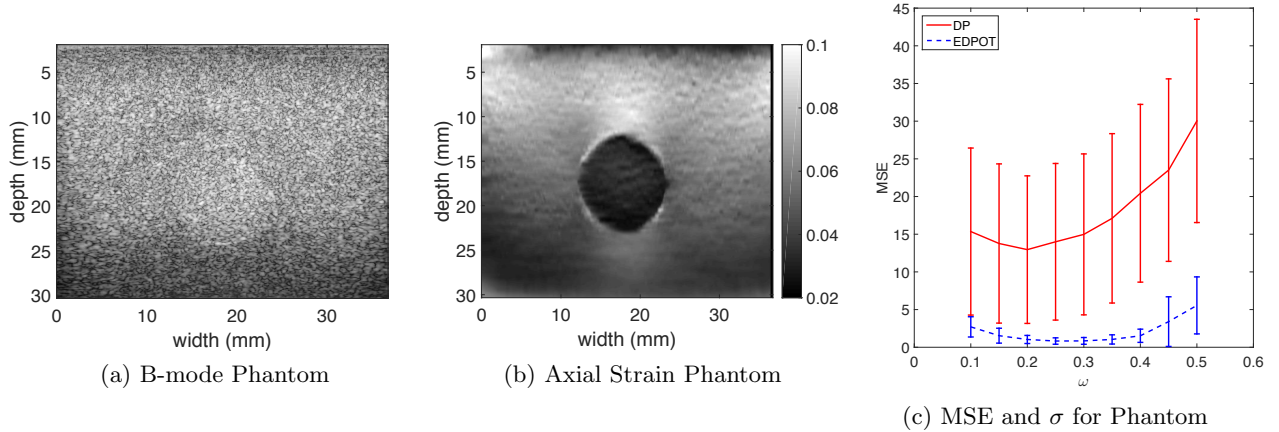


Figure 4: Images of the experimenting data sets. (a) shows the B-mode ultrasound image of the Phantom. (b) shows the axial strain where the DP method has not failed and in (c), the MSE of DP and ED POT are compared. $\sigma/10$ is used in error bars to ease comparison.

The main part of the program, i.e. performing DP on the tree and calculating displacements, was written in C++ and used as a Matlab MEX function. The data processing was done on a 3.40 GHz Core i7 quad core computer. For a 1000×100 ultrasound image, ED POT takes approximately 0.070 seconds to run on this

Table 1: The MSE and the standard deviation of the squared error for the Phantom, Patient 1 and Patient 2

Phantom										
w	0.1	0.15	0.2	0.25	0.3	0.35	0.4	0.45	0.5	
DP	15.35 ± 110.81	13.77 ± 105.62	12.95 ± 97.90	14.00 ± 103.89	14.98 ± 106.77	17.11 ± 112.36	20.43 ± 117.92	23.51 ± 121.08	30.03 ± 134.84	
EDPOT	2.71 ± 13.43	1.54 ± 9.88	1.03 ± 5.37	0.83 ± 4.23	0.85 ± 4.47	1.04 ± 6.10	1.52 ± 8.76	3.40 ± 32.95	5.55 ± 37.82	
Patient 1										
w	0.1	0.15	0.2	0.25	0.3	0.35	0.4	0.45	0.5	
DP	0.49 ± 3.37	0.43 ± 1.99	0.40 ± 1.75	0.40 ± 1.76	0.41 ± 1.80	0.42 ± 1.85	0.42 ± 1.89	0.43 ± 1.90	0.43 ± 1.91	
EDPOT	0.32 ± 1.20	0.29 ± 1.03	0.28 ± 1.01	0.27 ± 0.97	0.26 ± 0.86	0.27 ± 0.87	0.26 ± 0.85	0.26 ± 0.86	0.26 ± 0.86	
Patient 2										
w	0.1	0.15	0.2	0.25	0.3	0.35	0.4	0.45	0.5	
DP	4.35 ± 11.23	4.84 ± 11.58	5.52 ± 12.61	5.95 ± 13.00	6.39 ± 13.44	6.67 ± 13.57	7.37 ± 14.66	8.11 ± 15.82	9.18 ± 17.84	
EDPOT	4.17 ± 11.44	4.45 ± 11.68	4.74 ± 12.32	4.97 ± 12.66	5.25 ± 13.29	5.28 ± 13.24	5.59 ± 13.88	5.93 ± 14.61	8.50 ± 31.17	

machine, which is approximately 48.5% more than that of the previous method. Our implementation can be further optimized to reduce this time.

We compare the results of EDPOT with those of Ref. 8 (DP). In order to measure the improvement of EDPOT over DP, a ground truth displacement field is required. As mentioned before, failure in DP primarily depends on the choice of seed-line: if shadowing artifact, large out-of-plane or lateral motion, blood vessels or cysts are present at the seed-line, DP will likely fail. Failure in DP results in distinct errors in the displacement and strain images (Figure 1), and as such, is easy to detect by visual inspection. Therefore, to generate the ground truth, we run DP on multiple seed-lines and visually select a correct strain image. We use this displacement image as a ground truth displacement estimate. Note that while this ground truth is not perfect, it provides sufficient accuracy for our purpose of finding large displacement errors (Figure 1).

In the next step, for every RF-line, ID was calculated with that RF-line as the seed-line. With the ground truth at hand, we measured the error for both methods in terms of Mean Squared Error (MSE). We then report the mean and the standard deviation of the squared error for all seed-lines.

As stated in the Methods Section, the impact of the regularization term on the cost function is governed by w . Thereby, we calculated the displacements for a range of w ; from 0.1 to 0.5 with 0.05 increments. It is worth mentioning that due to the low lateral resolution of ultrasound images, we do not show lateral displacement results. Experimental results are provided below.

3.1 Phantom Experiments

The phantom data was acquired from a CIRS (Norfolk, VA) breast phantom. The data was collected with an Antares Siemens system (Issaquah, WA) at a center frequency of 6.67 MHz using A VF10-5 linear array with a 40MHz sampling rate. A B-mode image, a strain sample of the phantom data along with a strain can be seen in Figure 4. The MSE and standard deviation for a range of w is depicted in Figure 4c, and the numerical values are reported in Table 1.

3.2 Results On Patients With Liver Cancer

The data was collected from two patients with primary or secondary liver cancer who underwent open surgical radio-frequency thermal ablation. Data collection was performed at Johns Hopkins Hospital and was approved by its ethics board. These patients had unresectable disease and were recommended for RF ablation after review from Johns Hopkins University multidisciplinary conference. The RF data was acquired from an Antares Siemens system (Issaquah, WA) at the center frequency of 6.67 MHz with a VF10-5 linear array at a sampling rate of 40 MHz. Further details of the data acquisition are available in Ref. 8. B-mode images, strain images without any artifact and with artifact for Patient 1 and Patient 2 are depicted in Figure 5. The comparison of DP and EDPOT is also presented in Figure 6.

3.3 Estimating Tendon Displacement

Analyzing motion pattern of the tendons during passive motion or active contraction can provide invaluable tissue properties and is therefore of significant clinical interest. B-mode images of the patellar tendon of a healthy volunteer was collected using an Aplio 500 ultrasound machine with a 14 MHz frequency linear probe (Toshiba Medical Systems, Tokyo, Japan). This study is approved by the ethics boards of both McGill University

Health Center and Concordia University. The probe is hand-held, and is used to slowly push the tendon (visible at the top part of Figure 7a) down. Axial and lateral displacements are shown in parts (b) and (c) and depict an expected motion pattern. It is important to note that these high quality motion patterns are estimated from B-mode data, and are expected to significantly improve with RF data.

4. CONCLUSION

In this work we proposed a new method wherein the integer displacement is calculated for pixels on a tree, contrary to the previous work which was calculated on a single vertical line. This resulted in utilizing more information and thus improved the accuracy of the integer displacement field. This was confirmed with testing on RF data acquired from a phantom and also *in-vivo* human data. The proposed method was shown to significantly outperform the traditional DP. Lastly, a new application for estimation of tissue displacement using ultrasound was proposed for patellar tendon, which can lead to improved classification of tendon pathology and might help assess the healing process.

5. ACKNOWLEDGMENT

The authors would like to thank The Richard and Edith Strauss Canada Foundation for funding this project. The liver data was collected when H. R. was a student at Johns Hopkins University as a collaborative work with

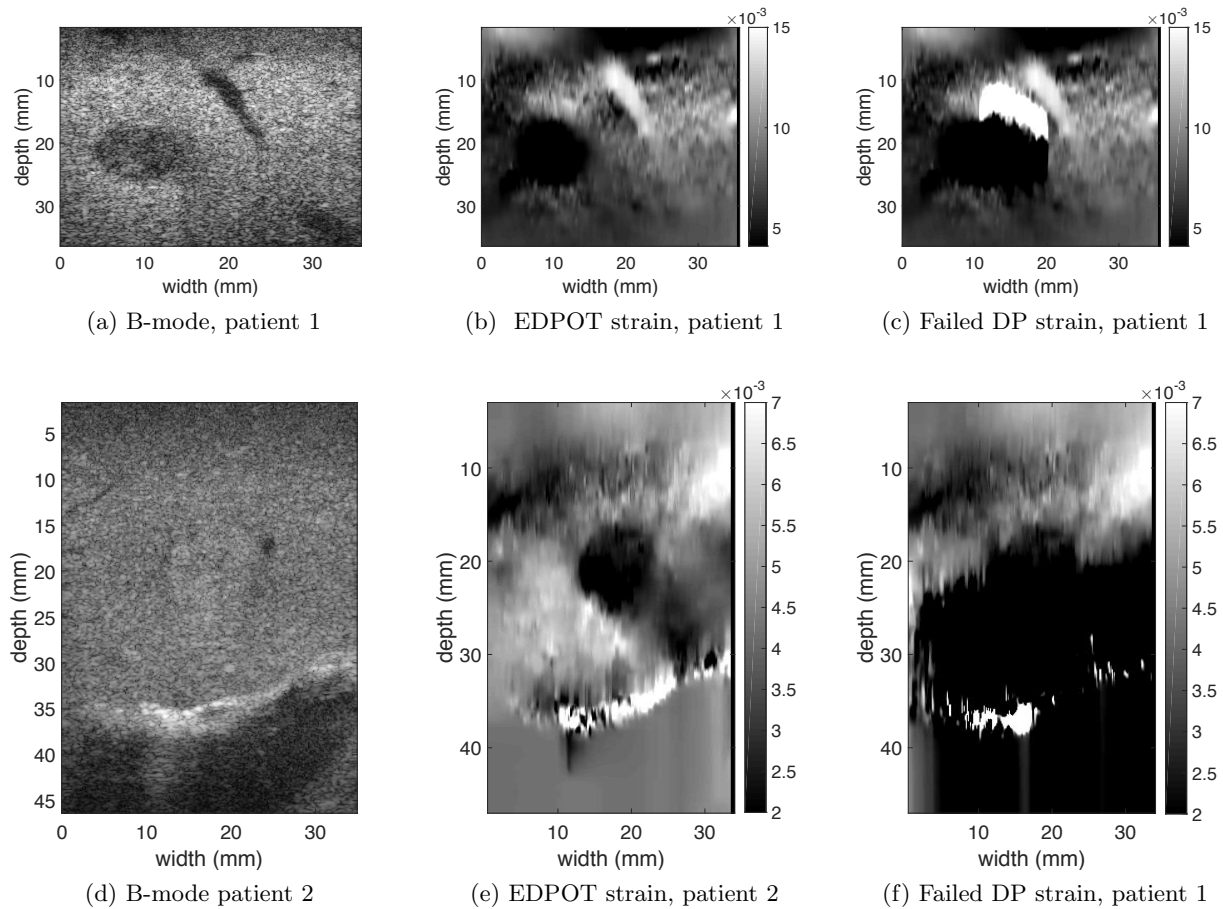


Figure 5: *In-vivo* images of human data. (a) and (d) show the B-mode ultrasound images of patient 1 and patient 2. (b) and (e) show the axial strains where the DP method has not failed and (c) and (f) show where DP has failed.

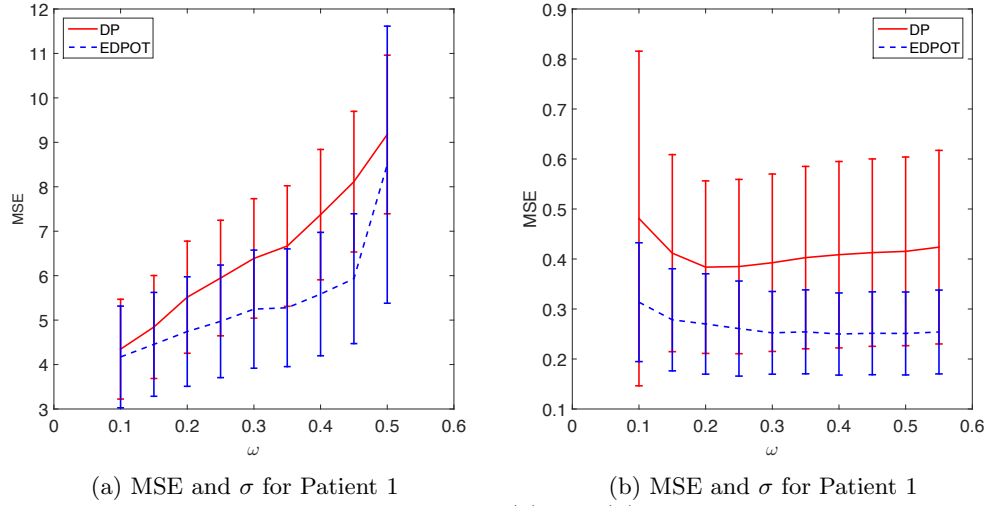


Figure 6: Comparing the result of DP and EDPOT. In (a) and (b) the MSE of DP and EDPOT are compared for Patient 1 and 2 respectively. For better comparison, $\sigma/10$ is shown.

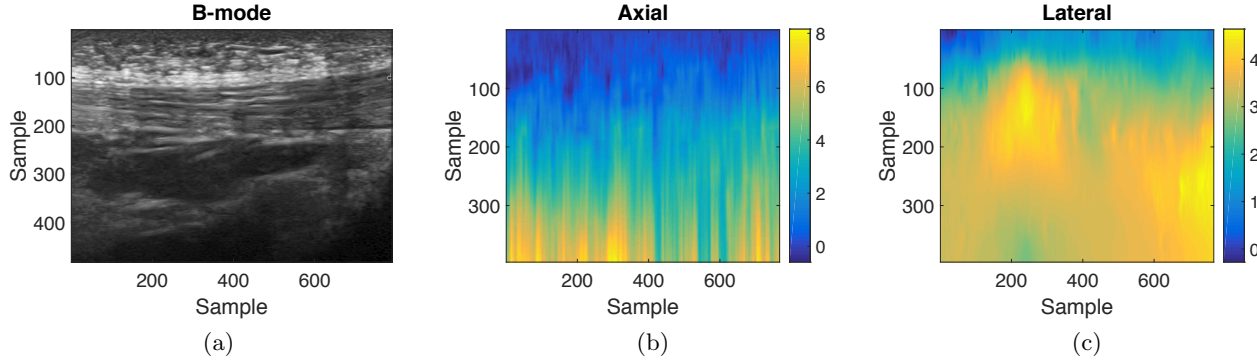


Figure 7: Results of *in-vivo* patellar tendon. (a) shows the B-mode of the patellar tendon which itself can be seen in the upper half of the image. (b) and (c) show the axial and lateral displacement during contraction

Drs. E. Boctor, G. Hager and M. Choti. The authors would like to thank E. B. , G. H. and M. C. for allowing us to use this data.

REFERENCES

- [1] Ophir, J., Alam, S. K., Garra, B., Kallel, F., Konofagou, E., Krouskop, T., and Varghese, T., "Elastography: ultrasonic estimation and imaging of the elastic properties of tissues.," *Proceedings of the Institution of Mechanical Engineers. Part H, Journal of engineering in medicine* **213**, 203–233 (1999).
- [2] Lu, M., Wu, D., Lin, W.-h., Li, W., Zhang, H., Huang, W., et al., "A stochastic filtering approach to recover strain images from quasi-static ultrasound elastography," *Biomedical engineering online* **13**(1), 15 (2014).
- [3] Kuzmin, A., Zakrzewski, A., Anthony, B., and Lempitsky, V., "Multi-frame elastography using a handheld force-controlled ultrasound probe," *Ultrasonics, Ferroelectrics, and Frequency Control, IEEE Transactions on* **62**, 1486–1500 (August 2015).
- [4] Rivaz, H., Boctor, E. M., Choti, M. a., and Hager, G. D., "Ultrasound elastography using multiple images," *Medical Image Analysis* **18**(2), 314–329 (2014).
- [5] Xia, R., Tao, G., and Thittai, A. K., "Dynamic frame pairing in real-time freehand elastography.," *IEEE transactions on ultrasonics, ferroelectrics, and frequency control* **61**(6), 979–85 (2014).

- [6] Jiang, J. and Hall, T., “6f-3 a regularized real-time motion tracking algorithm using dynamic programming for ultrasonic strain imaging,” in [*Ultrasonics Symposium, 2006. IEEE*], 606–609 (Oct 2006).
- [7] Rivaz, H., Boctor, E., Foroughi, P., Zellars, R., Fichtinger, G., and Hager, G., “Ultrasound elastography: A dynamic programming approach,” *IEEE Transactions on Medical Imaging* **27**(10), 1373–1377 (2008).
- [8] Rivaz, H., Boctor, E. M., Choti, M. a., and Hager, G. D., “Real-Time Regularized Ultrasound Elastography,” *IEEE Transactions on Medical Imaging* **30**(4), 928–945 (2011).
- [9] Fleming, I., Rivaz, H., Boctor, E., and Hager, G., “Robust dynamic programming method for ultrasound elastography,” in [*SPIE Medical Imaging*], 83201K–83201K, International Society for Optics and Photonics (2012).
- [10] Veksler, O., “Stereo correspondence by dynamic programming on a tree,” in [*Computer Vision and Pattern Recognition, 2005. CVPR 2005. IEEE Computer Society Conference on*], **2**, 384–390 vol. 2 (June 2005).